Development and application of a multi-scale modelling framework for urban high-resolution NO$_2$ pollution mapping

Zhaofeng Lv[1,★], Zhenyu Luo[1,★], Fanyuan Deng[1], Xiaotong Wang[1], Junchao Zhao[1], Lucheng Xu[1], Tingkun He[1],

Yingzhi Zhang[2], Huan Liu[1,*], Kebin He[1]

[1]State Key Joint Laboratory of ESPC, School of Environment, Tsinghua University, Beijing 100084, China

[2]College of Ecology and Environment, ChengDu University of Technology, Chengdu 610059, China

★Z. Lv. and Z. Luo. contributed equally to this work.

Corresponding Author:

*Phone and fax: 86-10-62771679; e-mail: liu_env@tsinghua.edu.cn.

Abstract. Vehicle emissions have become a major source of air pollution in urban areas, especially for near-road environments, where the pollution characteristics are difficult to be captured by a single-scale air quality model due to the complex composition of the underlying surface. Here we developed a hybrid model CMAQ-RLINE_URBAN to quantitatively analyse the effects of vehicle emissions on urban roadside NO$_2$ concentrations at a high spatial resolution of 50 m $\times$ 50 m. To estimate the influence of various street canyons on the dispersion of air pollutants, a Machine Learning-based Street Canyon Flow (MLSCF) scheme was established based on Computational Fluid Dynamic and two machine learning methods. The results indicated that compared with the CMAQ model, the hybrid model improved the underestimation of NO$_2$ concentration at near-road sites with MB changing from -10 μg/m^3 to 6.3 μg/m^3. The MLSCF scheme obviously increased upwind concentrations within deep street canyons due to changes in the wind environment caused by the vortex. In summer, the relative contribution of vehicles to NO$_2$ concentrations in Beijing urban areas was 39% on average, similar to results from CMAQ-ISAM model, but increased significantly with the decreased distance to the road centerline, especially reaching 75% on urban freeways.

25 **Graphical abstract.**

NO₂ map at high resolution

Coarse NO₂ map

Wind fields of
street canyons

Urban thermodynamic scheme
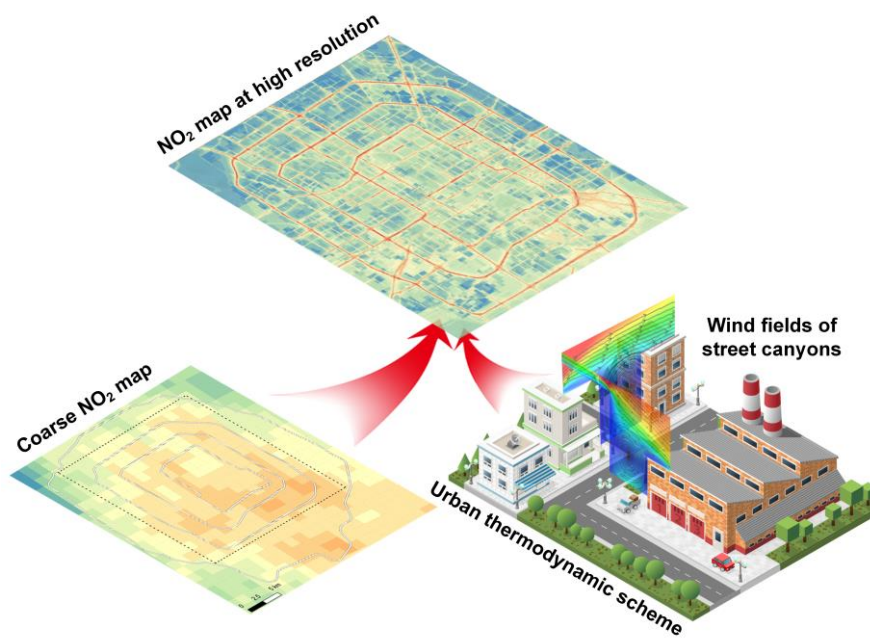
1 Introduction

The accelerated urbanization leads to severe air pollution in China. As one of the indicators of air pollution, nitrogen dioxide (NO_2) causes an adverse impact on human health and promotes the generation of ozone and particulate matter (Pandey et al., 2005; Khaniabadi et al., 2017). During the last decade, benefiting from the implementations of several air pollution control strategies by the Chinese government, the air quality has improved (Jin et al., 2016; Zheng et al., 2018), and the vertical column densities of NO_2 displayed a decreasing trend after 2013 (Shah et al., 2020; Cui et al., 2021). However, the economic development and nitrogen oxides (NO_x) emissions are not decoupled in China (Luo et al., 2022a). In some megacities of China, such as Chengdu, the daily averaged NO_2 concentration could reach 200 μg/m^3 (Zhu et al., 2019), far exceeding the 24-h average air quality guideline of 80 μg/m^3 suggested by the Ministry of Environmental Protection of China.

The improvement of $PM_{2.5}$ in China was mainly due to the emission reduction and control measures of industrial and domestic sources (Zhang et al., 2019b), which also relieved the NO_2 pollution, but the reduction potential of these sources has been gradually declining. Meanwhile, as the population of vehicles is growing rapidly, vehicle emissions have become a major source of NO_2 pollution, especially in urban areas (Nguyen et al., 2018). Due to the low release height of vehicle emissions, combined with the negative dispersion condition caused by nearby buildings, air pollutants will be significantly accumulated near the street. According to roadside observations, within the distance of about 100-200 m near roads, the concentrations of CO, NO_2, ultrafine particulate matter (UFP), $PM_{2.5}$, PM_{10}, and other pollutants will increase with the decreased distance to the road centerline, especially for the pollution levels of NO_2 and UFP increasing exponentially. Therefore, the gradient of concentration around the road changes dramatically (Nayeb Yazdi et al., 2015; Hagler et al., 2012). Moreover, the dispersion of air pollutants in the near-road environment is significantly affected by geometric characteristics of the street canyon. For example, in a standard street canyon, when the external wind direction at the roof level is perpendicular to the street axis, a clockwise vortex will be generated inside, resulting in the accumulation of pollutant concentrations at the upwind grid receptors in the canyon (Oke, 1988; Manning et al., 2000). Consequently, how to quantitatively identify urban vehicle-induced air pollution around roads affected by complex underlying surface conditions has become an urgent scientific issue.

Regional-scaled air quality models, represented by Chemical Transport Models (CTMs) including Community Multi-scale Air Quality (CMAQ) model (Byun and Schere, 2006), Comprehensive Air quality Model with

extensions (CAMx), and Weather Research and Forecasting/Chemistry model (WRF-Chem) (Grell et al., 2005), have been used extensively in assessment on the impacts of vehicle emissions on the regional atmospheric environment, focusing on the source apportionment (Luo et al., 2022b; Vara-Vela et al., 2016; Kheirbek et al., 2016; Lv et al., 2020) and evaluation of control measures (Zhang et al., 2020; Yu et al., 2019; Cheng et al., 2019; Ke et al., 2017). However, the spatial resolution of CTMs is generally larger than 1 km×1 km, so the significant impacts of vehicle emissions on near-source air quality cannot be predicted by CTMs due to the grid homogenization on vehicle emissions.

To avoid the aforementioned disadvantages, the local-scaled numerical models based on Gaussian diffusion theory or computational fluid dynamic (CFD) are adopted by numerous researches to study at a finer spatial resolution (Zhang et al., 2021b; Patterson and Harley, 2019; Soulhac et al., 2012), including Research LINE-source Dispersion Model (RLINE) (Snyder et al., 2013), Operational Street Pollution Model (OSPM), AERMOD (Cimorelli et al., 2005), and RapidAir® (Masey et al., 2018). However, the large uncertainties in predictions from Gaussian dispersion models come from the provided meteorological conditions and background concentrations. The natural logarithm function is usually used to characterize the vertical profile of wind speed in both the inertial and rough sublayers, neglecting the influence of urban complex underlying surface compositions on the wind field (Cimorelli et al., 2005; Masey et al., 2018; Snyder et al., 2013). Nevertheless, in standard and deep street canyons, the changes of vertical wind profile cannot be described by the logarithmic form, otherwise the actual wind speed will be greatly overestimated (Soulhac et al., 2008). Although the OSPM has performed a large number of comparisons with field observations in shallow or standard street canyons, the validation of model performance in deep street canyons with a large aspect ratio was still inadequate (Kakosimos et al., 2010). Moreover, OSPM overestimated the bottom wind speed in a deep street canyon by about 10 times compared with the predictions from CFD, resulting in greatly underestimating pollutant concentrations (Murena et al., 2009). Comparatively speaking, CFD model can accurately simulate the air flow and pollutant concentration in complex street canyons, but the simulation domain of CFD model is much smaller than the urban scale, and the influence of the long-term meteorological boundary conditions cannot be considered.

Considering the respective strengths and limitations of regional models and local models, several studies have been carried out on coupling of air quality models applicable to different scales (Ketzel et al., 2012; Stocker et al., 2012; Lefebvre et al., 2013; Jensen et al., 2017; Kim et al., 2018; Mallet et al., 2018; Hood et al., 2018; Benavides et al., 2019; Kamińska, 2019; Mu et al., 2022). Although these models performed accurately in near-road simulation, the

influence of street canyons is still hard to be considered. In some hybrid models (Stocker et al., 2012; Jensen et al., 2017; Mallet et al., 2018), OSPM was still applied to calculate concentration levels within the street, where the application of logarithmic wind profile probably overestimated the bottom wind speed in a deep street canyon as abovementioned. Other models simply assumed that in street canyons, wind direction followed the street direction, and wind speed was uniform, which was not sufficient to resolve the concentration gradient within street canyons (Kim et al., 2018; Benavides et al., 2019). Berchet et al. (2017) proposed a cost-effective method for simulating city-scale pollution taking advantage of high-resolution accurate CFD, while the primary NO_x was predicted due to the lack of a chemical module. Therefore, it is essential to build an integrated model to predict long-term and near-road air pollution suitable for the urban complex underlying surface environment.

In this paper, we developed a hybrid model CMAQ-RLINE_URBAN by offline coupling the local RLINE model with the regional CMAQ model and some localized urban thermodynamic parameter schemes, to simulate the near-road NO_2 pollution and quantify the impacts of vehicle emissions at a high spatial resolution. Specifically, in order to predict the effects of urban street canyons on the diffusion of pollutants, we developed a Machine Learning-based Street Canyon Flow (MLSCF) parameterization scheme, which was based on two machine learning methods using wind data from 1,600 CFD simulations. To evaluate the performance of CMAQ-RLINE_URBAN, simulations under several scenarios were conducted in Beijing urban areas from August 1st to 31th of 2019, and validated through comparison with observations from monitoring sites. Furthermore, spatial distribution characteristics of NO_2 concentrations in the near-road environment were also analysed in this study.

2 Materials and Methods

2.1 Hybrid model framework

Here, we established the MLSCF scheme based on R language, and modified the code of RLINE model to add other parameterization schemes with FORTRAN language. Finally, a multiscale air quality hybrid model was developed to achieve a high-resolution NO_2 pollution mapping in urban areas. The framework of CMAQ-RLINE_URBAN is shown in Figure 1. The hybrid model was established based on RLINE model, offline coupling with the gridded meteorological field provided by WRF model and the pollutant background concentrations from non-vehicle sources provided by CMAQ model with the Integrated Source Apportionment Method (ISAM), considering the thermodynamic effects caused by the complex underlying surface compositions of the city. In our model, a NO_2 pollution map with a high temporal (1 h) and spatial resolution (50 m×50 m) can finally be obtained.

119 RLINE is a Gaussian line source dispersion model developed by Snyder et al. (2013) to predict pollutant
120 concentrations in near-road environments. In the RLINE model, the mobile source is considered as a finite line
121 source, from which the concentration is found by approximating the line as a series of point sources and integrating
122 the contributions of point sources using an efficient numerical integration scheme. The number of points needed
123 for convergence to the proper solution is a function of distance from the source line to the receptor, and each point
124 source is simulated using a Gaussian plume formulation. The RLINE model performs generally comparable results
125 when evaluated with other line source models for on-road traffic emissions dispersion (Snyder et al., 2013; Heist
126 et al., 2013; Chang et al., 2015), and has been successfully used in many studies to evaluate the impacts from traffic
127 emissions on air quality (Zhai et al., 2016; Valencia et al., 2018; Benavides et al., 2019; Filigrana et al., 2020;
128 Zhang et al., 2021a).

129

130 The simulation for local meteorological conditions in CMAQ-RLINE_URBAN included three steps: Estimation
131 for areas above the top of Urban Canopy Layer (UCL), inside of UCL, and inside of the street canyon. (1) In this
132 study, the configuration of WRF model referred to our previous study (Lv et al., 2020). The height of midpoint in
133 the bottom layer to the ground was set as 22.5 m, which was close to the average height of buildings near street
134 canyons, similar to the settings in the previous study (Benavides et al., 2019). Therefore, the meteorological field
135 simulated by the WRF model was used as the wind field and atmospheric stability at the top of UCL. During the
136 hybrid model running, the meteorological conditions over buildings near each road were obtained separately from
137 WRF model according to the road location. (2) Then, the surface roughness length (z_0) of each road was estimated
138 based on the surrounding building geometry and used to recalculate the localized meteorological parameters (e.g.
139 Monin-Obukhov length) within UCL according to the algorithm proposed by Benavides et al. (2019) (z_0 scheme).
140 The atmospheric turbulence intensity in urban areas around sunset in the afternoon was obviously enhanced
141 considering the influence of the urban heat island effect based on methods in the AERMOD model (Cimorelli et
142 al., 2005) (UHI scheme). The UHI scheme would affect the turbulent intensity based on the evaluation for the
143 upward surface heat flux and the urban boundary layer height due to convective effects, and then the mixing height,
144 convective velocity scale, surface friction velocity, and Monin-Obhukov length were all recalculated (details in the
145 Supplement Section S1). (3) Finally, the wind field within UCL was calculated according to different types of road
146 environments: open terrain and street canyon. The logarithmic wind profile based on Monin-Obhukov Similarity
147 Theory (MOST) (Foken, 2006) in the original RLINE model was still used when the grid receptor was located in
148 the open terrain (MOST scheme), while the MLSCF parameterization scheme was used for grid receptors within
149 the street canyon to quantitatively characterize the influence of the street canyon geometry and the external wind

150 environment at the top of the roof. The detailed introduction for street canyon geometry and the MLSCF scheme

151 was described in the following section.

152

153 The real-time vehicle emission inventory based on Street-Level On-road Vehicle Emission (SLOVE) Model

154 developed in our previous study (Lv et al., 2020), which was based on the real-time traffic condition data from

155 AMap, was used in both regional and local air quality models. In our simulation, the concentrations of NO, NO_2,

156 and O_3 excluding contributions from vehicle emissions were used as background concentrations at the roof level,

157 avoiding the double counting in the coupling process. These background concentrations were simulated by CMAQ-

158 ISAM model, in which the emissions were divided into mobile and other four emission groups to trace their

159 contributions separately, and details were presented in our previous study (Lv et al., 2020). In addition, the influence

160 of atmospheric turbulence and building geometry on the vertical mixing of background concentration was

161 considered (vertical mixing scheme). The ratios of wind speed at surface and roof levels were used as a proxy to

162 calculate the contribution of background concentration over street canyons to the near-ground level (Benavides et

163 al., 2019). In this scheme, the surface wind was from MLSCF scheme when the gird receptor is located within the

164 street canyon, and otherwise the logarithmic wind profile was used to calculate the wind speed at the specified

165 height, and details were showed in the Supplement Section S2. Finally, combined with the vehicle-induced primary

166 NO_x concentration calculated by the RLINE kernel, the high spatial resolution NO_2 map could be simulated

167 considering the photochemical process of NO_x. In this study, a simplified two-reaction scheme, including the

168 photolysis of NO_2 and the oxidation of NO, was incorporated into the model to characterize the photochemical

169 process of NO_x (details in the Supplement Section S3), which has been successfully applied in the SIRANE

170 dispersion model (Soulhac et al., 2017).

171

172 **2.2 Development for MLSCF scheme**

173 **2.2.1 The database of street canyon geometry**

174 We first established a database of street canyon geometry for 15,398 roads in urban areas of Beijing based on the

175 three-dimensional building data obtained from our previous study (Lv et al., 2020) using Geographic Information

176 System (GIS). Three typical parameters to represent street canyon geometry were investigated, including height

177 ratio (H_l/H_r) (H_l is the building height on the left side, while H_r is the building height on the right side), aspect

178 ratio (H/W) (H is set to be the average height, and W is the width of the street canyon), the canyon length to height

179 ratio (L/H) (L is set to be the length of the street canyon). In this study, the extremely special geometry of canyons

180 was not considered, and the typical street canyons were selected as the following conditions: (1) The proportion of

181 actual street canyon length (the length of road where the buildings nearby) was greater than 0.5; (2) H/W was

182 greater than 0.2; (3) H_l/H_r was between 0.3 and 3.3. Finally, the total number of the typical street canyon was

183 1,889, with a total length of 787 km. The spatial distributions of canyon geometry are shown in Figure S1 in the

184 Supplement. In urban areas of Beijing, street canyon was generally wide with the averaged width of 50.3 m, and

185 buildings on both sides were relatively low with a mean of 23.6 m. Most street canyons were obviously located in

186 areas within the fourth ring road. The shallow ($H/W \leq 0.5$) canyons and long canyons ($L/H > 7$) were dominated,

187 accounting for 54% and 84% of the total number of street canyons.

188

189 **2.2.2 Description of CFD cases**

190 Here, to predict air flow in street canyons comprehensively, CFD simulations were conducted under combinations

191 of different values of controlling factors based on ANSYS FLUENT (v19.2). The controlling factors included the

192 aforementioned three typical parameters to represent canyon geometry, the background wind speed at the height of

193 H ($V(H)$) and the angle between wind direction and street axis (α) to describe the external wind environment. The

194 selected values of each factor were listed in Table 1, and total 1600 (i.e., 5×4×4×5×4) simulations were

195 implemented.

196

197 In this study, the computational domain of three-dimensional (3D) full-scale CFD simulations is shown in Figure

198 2. The average building height H of the street canyon was always set to 21 m in different simulations, which was

199 similar to the mean street canyon height in Beijing. Other actual size of street canyons (e.g. street canyon width W)

200 was calculated according to the ratio of each specific simulation. Distances between urban canopy layers (UCL)

201 boundaries and the domain top, domain inlet and domain outlet were set as $5H$, $6H$, and $20H$, respectively.

202

203 The turbulence closure schemes for CFD include the Reynolds-Averaged Navier-Stokes (RANS) and the Large-

204 Eddy Simulation (LES), and the choice of them depends on the computational cost, the accuracy required and the

205 purpose of application. The RANS resolves the mean time-averaged properties with all the turbulence motions to

206 be modelled, while LES adopts a spatial filtering operation and consequently resolves large-scale eddies directly

207 and parameterizes small-scale eddies (Zhong et al., 2016). Compared with the LES, the RANS is more easily

208 established and computationally faster (Xie and Castro, 2006). However, the LES can provide a better prediction

209 of air flow than that from the RANS when handling complex geometries (Dejoan et al., 2010; Santiago et al., 2010).

210   In this study, considering the huge computational burden of a large number of simulations and the relatively simple

211   geometry of street canyons in our modelling, the RANS was selected to characterize the air flow.

212

213   Following the CFD guideline (Tominaga et al., 2008; Franke et al., 2011), zero normal gradient conditions or

214   pressure outlet conditions were applied at the domain outlet, and symmetry boundary conditions were adopted at

215   the domain top and two lateral domain boundaries. For near-wall treatment, no-slip wall boundary conditions with

216   standard wall functions were used (Fluent, 2006). All governing equations for the flow and turbulent quantities

217   were discretized by the finite volume method with the second-order upwind scheme. The SIMPLE scheme was

218   used for the pressure and velocity coupling. The residual for continuity equation, velocity components, turbulent

219   kinetic energy, and its dissipation rate were all below 10^{-5}. Meanwhile, the CFD simulation would also stop when

220   the iteration steps exceeded 10,000, due to the large computing cost of so many simulations. The selected turbulence

221   model and grid arrangement are discussed in the following section.

222

223   At the domain inlet, the power-law velocity profile (Brown et al., 2001), vertical profiles of turbulent kinetic energy

224   k_{in} and its dissipation rate ε_{in} at the domain inlet (Lien and Yee, 2004; Zhang et al., 2019a), were described below:

225
$$U_0(z) = U_{ref} \left(\frac{z}{H_{ref}} \right)^{\alpha}$$

226
$$k_{in}(z) = \left(I_{in} \times U_0(z) \right)^2$$

227
$$\varepsilon_{in}(z) = \frac{C_\mu^{3/4} k_{in}^{3/2}}{\kappa z}$$

228   Here, $U_0(z)$ stood for the stream-wise velocity at the height z. U_{ref} represented the reference speed. The reference

229   height H_{ref} was 21m. The power-law exponent of α=0.22 denoted underlying surface roughness above medium-

230   dense urban area (Kikumoto et al., 2017). Turbulence intensity I_{in} was 0.1, Von Karman constant κ was 0.41 and

231   C_μ was 0.09.

232

233   **2.2.3 The CFD validation**

234   In this study, the stream-wise and vertical velocity predicted by CFD within street canyons was compared with

235   wind tunnel data in previous researches. For buildings of the cube arrays model, wind tunnel data from Brown et

236   al. (2001) was used to evaluate the reliability of CFD results by measuring vertical profiles of velocity. In this

237   experiment, street canyon was perpendicular to the wind direction at the roof level. For long-street models, we

238   predicted horizontal profiles of velocity along the street centerline at the height of z=0.11H or vertical profiles at

239   some points and then validated CFD simulations using wind tunnel data from Hang et al. (2010). In this validation

240   case, the wind direction at the roof level was parallel to the axis of street canyons. The description and validation

241   results are shown in Figure S2-S3, and Table S1 in the Supplement, respectively.

242

243   We identified the influence of different minimum sizes of hexahedral cells near wall surfaces (fine: 0.1m, medium:

244   0.2m, and coarse: 0.5m) and turbulence models (standard k-ε model and RNG k-ε model) on the predicted velocity,

245   to evaluate the grid independence and turbulence model accuracy (Figure S3 in the Supplement). The results

246   indicated that the predictions from the standard k-ε model could well match the variations of observed velocity

247   within the street canyon, of which performances were much better than that of the RNG model. In addition, different

248   grid resolutions used in simulations would not obviously affect the predicted results. We finally adopted the

249   standard k-ε model to characterize turbulence, and the grid with an expansion ratio of 1.1 was applied in which the

250   minimum size of hexahedral cells near wall surfaces was 0.5 m to save the computing cost.

251

252   Moreover, the averaged wind speed from CFD in street canyons with different aspect ratios and external wind

253   direction was compared with predictions from other empirical methods used in SIRANE model (Soulhac et al.,

254   2012) and MUNICH model (Kim et al., 2018). Similar predictions using different methods also proved the

255   reliability of CFD simulation in this study (Figure S4 in the Supplement).

256

257   **2.2.4 Machine learning**

258   Data driven method, such as machine learning and deep learning, is now a successful operational geoscientific

259   processing schemes and has co-evolved with data availability over the past decade (Reichstein et al., 2019).

260   Specially, these models have been used as computationally efficient emulators of explicit mechanism models, to

261   explore uncertainties (Aleksankina et al., 2019) and sensitivities or replace complex gas-phase chemistry schemes

262   (Keller and Evans, 2019; Conibear et al., 2021). In addition, meta-models (Fang et al., 2005) such as neural

263   networks and Gaussian process (Beddows et al., 2017) are also used to produce a quick to run model surrogate and

264   show reliable performance. Random Forest (RF) model algorithm is an ensemble learning method that generates

265   many decision trees and aggregates their results, which has been developed to solve the high variance errors typical

266   of a single decision tree (Breiman, 2001). Multivariate Adaptive Regression Splines (MARS) is a nonparametric

267   and nonlinear regression method, which can be regarded as an extension of the multivariate linear model (Friedman,

268   1991). RF and MARS are common machine learning methods which run efficiently on large data sets, and are

269 relatively robust to outliers and noise. Furthermore, they never require the specification of underlying data model
270 and the complex parameter tuning, and they can still provide efficient alternatives and generally show a high
271 accuracy in applications for predict air pollutant concentrations (Hu et al., 2017; Chen et al., 2018; Kamińska, 2019;
272 Geng et al., 2020).

274 Here, based on the database including 42,880 samples obtained from 1600 CFD simulations, the RF and MARS
275 were both used to simulate the wind vector along X-axis (V_x) and Y-axis (V_y) at different heights within the street
276 canyon respectively. The input predictor variables included H/W, L/W, H_l/H_r, the grid receptor relative height
277 (z/H), the background wind vector at the height of H along X-axis ($Vbg_x = V(H) \times \sin\alpha$) and Y-axis ($Vbg_y =$
278 $V(H) \times \cos\alpha$). We finally combined the advantages of these two machine learning models and developed the
279 MLSCF scheme to predict wind environment in street canyons and incorporated into the hybrid model, which is
280 discussed in the section 3.1.

282 In RF model, the number of predictors randomly sampled at each split node in the decision tree (m_{try}) and the
283 number of trees to grow ($NumTrees$) are two important hyperparameters that determine the performance of the
284 model. Similarly, in MARS model, the two important hyperparameters are the total number of terms ($nprune$) and
285 the maximum number of interactions ($degree$). By comparing the mean squared error (MSE) for testing datasets
286 across models with candidate parameter combinations, we set m_{try} and $NumTrees$ as 6 and 200 in RF,
287 respectively, and $nprune$ and $degree$ as 23 and 3 in MARS, respectively. Additionally, the 10-fold cross-
288 validation (CV) repeated ten times were considered to evaluate the prediction performance of our models. The total
289 dataset was randomly divided into 10 subsets, where 9 subsets was used to train model and another was applied for
290 validation. The fitted coefficients of MARS are shown in Table S2-S3 in the Supplement.

292 In order to identify the sensitivity and response relationship between prediction variables and results in RF model,
293 we used the MSE for out-of-bag (OOB) to evaluate the relative importance of each feature to V_x and V_y, by
294 randomly replacing the value of a single prediction variable one by one (Liaw, 2002). Higher values of increase in
295 MSE indicated that the predictor was more important. In addition, Partial Dependence Plots (PDPs) was applied to
296 establish the response relationship between the change of a single predictive variable and the predicted results,
297 considering the average influence of other variables (Greenwell, 2017).

298

2.3 Configuration of CMAQ-RLINE_URBAN

The near-ground NO_2 concentrations were simulated from August 1st to 31th in 2019 when the average of daily high temperatures was higher than 30 ℃ and sunlight duration was longer than 13 hours, leading to strong photochemical reactions. The simulation domain for the hybrid model covered the core urban areas within and surrounding the fifth ring road, shown in Figure 3. The receptors included both grid receptors and monitor receptors. The grid receptors were set at a spatial resolution of 50 m×50 m, and the height above the ground was 1.5 m, which was equivalent to the height of the human breathing. We used data from 10 observation stations (monitor receptors) located in the normal urban environment and 5 near-road monitoring sites for validation (Beijing Ecological Environment Monitoring Center, available at http://zx.bjmemc.com.cn/) (DSH, NSH, QM, XZM, and YDM) in the simulation domain (Figure 3), which were 10 meters and 3 meters above the ground respectively. The QM and XZM sites were located in shallow street canyons, and details for the morphometric of near-road measurement sites were shown in Table S4 in the Supplement.

In general, compared to the RLINE model, CMAQ-RLINE_URBAN has the following improvements:

(a) The gridded meteorological parameters provided by WRF model were used.

(b) Gridded non-vehicle-related concentrations provided by CMAQ-ISAM model were used as background concentrations.

(c) A simple NO_x photochemical scheme was incorporated to simulate NO_2 concentrations.

(d) Thermodynamic effects caused by the special underlying surface structures of the city were considered, including UHI effects, the influence of local buildings on turbulence intensity and vertical mixing of background concentrations.

(e) A newly developed MLSCF scheme was applied to predict wind environment in street canyons.

In our simulation, the model configurations in the base scenario CMAQ-RLINE_URBAN included all (a)-(e) schemes, and the other two control scenarios were set to investigate the sensitivity of urban schemes on predictions, where all input data was set to be the same. The scenario CMAQ-RLINE only including (a)-(c) schemes was set to analyze the impacts of urban thermodynamic schemes, and the scenario CMAQ-RLINE_URBAN_nc including (a)-(d) schemes was set to identify the impacts of the MLSCF scheme.

3 Results

3.1 Fitting results of machine learning

In this study, the 10-fold cross-validation (CV) repeated ten times was considered to evaluate the prediction performances of RF and MARS models. As shown in Figure 4 and Figure S5, both models performed acceptable robustness in CV, indicating that neither RF nor MARS model overfitted the data. In general, the performances of both models in predicting V_y was better than that in V_x of which the absolute value was relatively small, especially for MARS model. Since V_x was responsible for the formation of the vortex within street canyons and affected by multiple factors, it was more difficult to be simulated. The averages of mean absolute error (MAE), root mean square error (RMSE), and correlation coefficient (R) in the CV of the RF model for V_x and V_y were 0.04 m/s and 0.05 m/s, 0.02 m/s and 0.03 m/s, and 0.99, respectively. Although the average of the relative error (RE) were a little high (42.5% and 43%), particularly when the predicted wind speed was low, the median RE were relatively low with 9.8% and 2.7%, respectively, indicating an acceptable performance. Compared with the advanced non-linear RF algorithm, the MARS model performed not very well, especially when the absolute value of V_x was greater than 1 m/s and V_y was less than 3 m/s. However, when the predicted wind speed by machine learning methods was compared with observations from wind tunnel experiments, we found that the performance of the MARS model was obviously better than that of RF model in one of validation cases (see Figure 5). The decision tree model like RF failed to respond to the parts beyond the range of prediction variables (Vbg_y=17 m/s >>5 m/s), while the more reasonable predictions can be obtained by the MARS model which used piecewise linear function essentially. Therefore, the MLSCF scheme was established based on a method to combine the advantages of each model. The RF model was used when the input value was within the range of predictors shown in Table 1, otherwise the predictions from the MARS model were used.

In addition, the importance of each predictor variable in the RF model was investigated to explain their impacts on predictions. As shown in Figure 6, the background wind speeds on x and y axis played vital roles in predictions of V_x and V_y, respectively, followed by the relative height (z/H). Among the geometric parameters of the street canyon, the impact of L/W was least. Since V_x was the main driving force for the formation of vortices in street canyons, it was more affected by the geometry of street canyons especially H_l/H_r, comparing to V_y. This feature importance ranking was basically consistent with the conclusion in a previous study (Fu et al., 2017). Figure S6 in the Supplement shows the PDPs of each predictor variable in RF model for V_x and V_y. As z/H grew, V_x and V_y showed linear and logarithmic increase patterns, respectively. And the resistant effect of windward buildings on

wind speed enhanced with the increasing of H_l/H_r, resulting in a significant decrease in V_x particularly when H_l/H_r was lower than 1.25. The relationship between predictors and results in the model was consistent with the actual mechanism, indicating our model could provide an accurate description of the wind field in the street canyon.

3.2 Impacts of MLSCF on simulations in street canyons

We compared the differences between monthly mean wind profile in different street canyons including QM (shallow canyon: $H/W = 0.22$), XZM (shallow canyon: $H/W = 0.35$), SZJ (standard canyon: $H/W = 1$) and JTDL (deep canyon: $H/W = 1.93$), calculated by the default logarithmic function based on MOST in the original RLINE model (Foken, 2006), and the MLSCF scheme developed in this study. As shown in Figure 7(a)-(d), the wind profile estimated by MOST showed a logarithmic change at the height above displacement height (d_h) with a decrease to 0 at d_h, and remained constant below d_h (the d_h is calculated by multiplying surface roughness length (z_0) times a factor which is recommended to be set as 5). Compared with the MOST, the simulated wind speeds near the ground and at the top of canyons were generally lower based on the MLSCF scheme in shallow and standard street canyons. In the deep street canyon, the significant reduction in ventilation volume led to the mean wind speed simulated by the MLSCF scheme much lower than that of MOST at all heights. Although the aspect ratios of the street canyon located in QM and XZM were similar, their orientations were quite different, resulting in significant differences under prevailing external winds in different directions. Since the prevailing northerly and southerly wind was observed in Beijing during the study period, the resistance effect of the buildings on both sides of the east-west street canyon located in QM was more obvious.

We also investigated the impacts of the MLSCF on hourly wind direction at the bottom ($z = 3m$) of different street canyons by comparing the roof-level predictions from WRF model (see Figure 7(e)-(f)). In the shallow street canyon like QM, the simulated wind direction at the bottom was consistent with the background on the whole, with the R reaching 0.8. When the background wind direction was less than 180°, the averaged wind direction at the bottom simulated by MLSCF was 91.8°, which was basically consistent with the angle between the street and the south direction (84.5°). When the background wind direction was greater than 180°, the average wind direction predicted by MLSCF (257.4°) was similar to that in the opposite direction of the street (264.5°), which was in line with the theory proposed by Soulhac et al. (2008) that the average wind direction in street canyons was assumed to be consistent with the (opposite) orientation of the street. While in the deep street canyon of SZJ, when the external wind perpendicularly blew to the street, the wind direction at the bottom was completely opposite to that at the top due to the formation of vortex, with the R reaching -0.97. In conclusion, compared with the traditional MOST

389 method, the newly developed MLSCF scheme could well simulate the influence of the external wind environment
390 and geometry on the wind field inside the street canyon.

391

392 As shown in Figure 8, the impacts of the MLSCF scheme on simulated NO_2 concentration were identified by the
393 differences between CMAQ-RLINE_URBAN and CMAQ-RLINE_URBAN_nc scenario during a clean day
394 (August 24th). When the atmosphere was stable at night, in street canyons with a large aspect ratio, the wind
395 direction at the bottom changed to the opposite to that at the top, combined with the decreased wind speed affected
396 by the MLSCF scheme, the NO_2 concentrations at upwind grid receptors increased by up to 80 μg/m^3. Meanwhile,
397 the changes in wind direction would also decrease the concentrations at downwind grid receptors by up to 20 μg/m^3.
398 For example, in the SZJ standard canyon, the background wind direction over the street was 79° (easterly), and
399 the wind direction at the bottom changed to 291° affected by the MLSCF scheme (westerly). Therefore, the upwind
400 NO_2 concentrations increased, and the location of peak NO_2 concentration shifted to the windward. Since the
401 changes in NO_2 concentrations were also influenced by the local on-road emissions, the increase was only up to
402 2.1 μg/m^3 in SJZ street, where the traffic flow and vehicle emissions were small at night. However, a little influence
403 was observed during the day in the convective boundary layer. During this period, although the wind direction at
404 the bottom was not changed obviously due to the parallel background wind in SZJ street, the increased surface
405 wind speed was beneficial for the dispersion, resulting in the decreased concentration in grid receptors within both
406 sides of the street canyon. In summary, the MLSCF scheme enabled the characterization of the concentration
407 distribution in street canyons.

408

409 **3.3 Performance of near-road simulations from different models**
410 The performances in predicting NO_2 concentrations at all monitor receptors from different models were first
411 compared, including CMAQ-RLINE_URBAN, CMAQ-RLINE and CMAQ model. The mean bias (MB), RMSE,
412 normalized mean bias (NMB), normalized mean gross error (NMGE), the fraction of predictions within a factor of
413 two (FAC2), Index of agreement (IOA), and *R* between simulations and observations were all selected as statistical
414 indicators for the evaluation (Table 2). In general, the performance of CMAQ-RLINE_URBAN was the best at all
415 urban sites. Compared to the CMAQ model, the averaged MB and NMB at urban sites in the hybrid model
416 decreased from 8 μg/m^3 to 1.3 μg/m^3 and 27% to 4%, respectively.

417

418 Diurnal variations of observed and predicted hourly averaged NO_2 concentrations at near-road sites from different
419 models were mainly compared and shown in Figure 9. The comparison of hourly and daily averaged concentrations

420 is shown in Figure 10. Overall, the CMAQ-RLINE_URBAN performed best with the smallest deviations. By
421 comparing the performances of the CMAQ and CMAQ-RLINE scenario, we found the direct coupling between the
422 CMAQ and RLINE models could reproduce the high NO_2 concentrations at near-road sites in daytime, and
423 significantly improve the underestimation of near-source concentrations due to grid dilution on emissions in
424 CMAQ model. The averaged MB and NMB at all sites changed from -10 $\mu g/m^3$ to 25.6 $\mu g/m^3$, and from -20% to
425 51%, respectively. However, a significant overestimation was found in the CMAQ-RLINE at night (0:00-6:00) and
426 around sunset in the afternoon (16:00-23:00), of which the peak could exceed the observed concentrations by more
427 than 1 times. This overestimation was reduced in the CMAQ-RLINE_URBAN, where the urban thermodynamic
428 schemes were implemented. The averaged MB and NMB decreased to 6.3 $\mu g/m^3$ and 12%, respectively, due to the
429 following reasons: (1) The increased surface roughness length slightly enhanced local turbulence intensity near
430 roads; (2) The UHI scheme enhanced the intensity of atmospheric turbulence in urban areas before and after sunset
431 in the afternoon; (3) The effect of turbulence intensity on the local vertical mixing of background concentrations
432 was considered, significantly reducing the mixing ratio of concentrations over UCL and near the ground at nights
433 in the stable boundary layer (Figure S7 in the Supplement), which was probably the main driving force of decreased
434 predictions in the hybrid model (Benavides et al., 2019). However, the CMAQ-RLINE_URBAN slightly
435 overestimated the nighttime NO_2 concentration of all observation stations except the DSH, which was probably
436 caused by overestimations of background concentrations from CMAQ-ISAM and vehicle emissions.

437

438 The accuracy of model performances at each traffic site showed a little difference affected by the variations in the
439 traffic flow and emissions of nearby roads, as well as the geometry of surrounding buildings and street canyons. At
440 DSH and NSH sites, which were adjacent to ring roads as the main urban freight corridors with a high traffic flow
441 including a large proportion of trucks, the high NO_x emissions led to the highest roadside NO_2 observations among
442 all sites. The CMAQ model would significantly underestimate the high NO_2 concentration at sites nearby ring roads,
443 with MB and NMB lower than -15 $\mu g/m^3$ and -28% (Table S5 in the Supplement), respectively, which was
444 improved using CMAQ-RLINE_URBAN. However, the hybrid model performed a minor overestimation at the
445 NSH site, since the monitor was actually positioned in the road centerline but assumed to be located downwind in
446 the model, resulting in a relatively large systematically error (Snyder et al., 2013). In total, CMAQ-
447 RLINE_URBAN performed best among all models, especially improving the estimation of NO_2 concentrations
448 near roads by the original regional model.

449

450   Additionally, Figure S8 in the Supplement shows the comparison between simulated and observed roadside hourly
451   and daily maximum 8-hour average O_3 concentrations by different models, and their diurnal variations are shown
452   in Figure S9. Generally, the hybrid model significantly improved the overestimation of daytime O_3 concentrations
453   by the CMAQ model when considering the titration effect of high NO concentration near roads on O_3. In the hybrid
454   model, the peak time was delayed to about 15:00, which was closer to the observation, but still 1-2 hours earlier
455   than the actual time, which may be related to the uncertainty in NO_2 photolysis rate.

456

457   **3.4 Spatial distribution characteristics of simulated concentrations**

458   We investigated the differences between the spatial distribution of the monthly averaged NO_2 concentration
459   simulated by the CMAQ and CMAQ-RLINE_URBAN models, as shown in Figure 11. Since the urban
460   thermodynamic schemes were considered in the hybrid model, the overestimation of most urban environmental
461   grid receptors by CMAQ model was relieved. Within the fourth ring road and its surrounding areas, the mean
462   concentration of NO_2 from CMAQ-RLINE_URBAN was 30.1 $\mu g/m^3$, lower than that from the CMAQ model (39.5
463   $\mu g/m^3$). The overall spatial distribution characteristics of NO_2 predictions from both models showed that the
464   concentrations in south regions were high due to the pollution transport from Hebei province (An et al., 2019).
465   However, near-road hotspots for the NO_2 pollution were identified in the hybrid model where the spatial resolution
466   of results increased to 50 m×50 m. The NO_2 concentrations nearby ring roads with high traffic flow and emissions
467   were up to 120 $\mu g/m^3$, much higher than the maximum prediction from CMAQ model (52.4 $\mu g/m^3$). In addition,
468   the simulated near-road concentrations from the hybrid model during traffic peak hours (18:00-19:00) were
469   significantly higher than those at noon (12:00-13:00), while there were few changes in results from CMAQ model
470   (Figure S10 in the Supplement).

471

472   The NO_2 concentrations estimated by CMAQ-RLINE_URBAN at all grid receptors grids followed a two-mode
473   Gaussian distribution (Figure S11 in the Supplement), which was similar to Zhang's results (Zhang et al., 2021b).
474   The NO_2 concentrations as a result of vehicle emissions were further calculated by the differences between the total
475   and background concentrations. In general, the vehicle-induced NO_2 concentrations in urban areas was 11.8 $\mu g/m^3$,
476   accounting for 39% of the total concentrations, which was similar to the predicted contribution from the CMAQ-
477   ISAM model (42.5%).

478

479   Figure 12 shows the changes in NO_2 concentrations simulated by the hybrid model with distance from the grid
480   receptors to its nearest road centerline. The concentrations at grid receptors within 200 m from road were

significantly affected by vehicle emissions. Within 50 m around the road, as the distance from grid receptors to the road centerline gradually increased, the NO_2 concentrations decreased exponentially. The total NO_2 concentrations decreased from 53.1 $\mu g/m^3$ to 30 $\mu g/m^3$, and the vehicle-induced concentrations also dropped from 34.7 $\mu g/m^3$ to 12.6 $\mu g/m^3$. The concentrations near roads with different types were highly dependent on the emission intensity. The NO_2 concentration was highest in the center of the urban freeway, which was 76 $\mu g/m^3$ and about 1.9 times higher than that on local roads. The relative contribution of vehicle emissions to NO_2 concentration reached up to 75.3% on urban freeways, as well as 71.9% and 65.5% on artery roads and freeways, but only 51.1% on local roads. It was worth noting that although the NO_2 concentrations at far grid receptors to the road on highways were slightly higher than those on other road types, the contribution of vehicle emissions was the least. It was since the NO_x emission intensity of freeways was as high as that on artery roads, but the density and height of buildings around freeways were usually low, resulting in a high vertical flux of background concentrations from the top of UCL to the ground. In conclusion, the results from the hybrid model accurately reflected not only the impacts of local on-road emissions, but also the pollution characteristics affected by non-vehicle sources at the regional scale.

4 Conclusion and Discussions

In this study, we developed a hybrid model CMAQ-RLINE_URBAN to quantitatively analyse the effects of vehicle emissions on urban roadside NO_2 concentrations at a high spatial resolution of 50 m × 50 m. The main conclusions of this study are as follows:

The developed MLSCF scheme revealed that affected by the geometry of buildings on both sides of the road, the wind filed in the street canyon sometimes was quite different from that in the environmental background. In deep street canyons, the wind speed at the bottom decreased obviously due to the resistant effect of buildings, and the directions of horizontal flow at bottom and top of the canyon were completely opposite due to the formation of vortex. The application of MLSCF scheme in the hybrid model led to increase NO_2 concentrations at upwind grid receptors within deep street canyons due to changes in the wind environment. However, the influence of the turbulence induced by street canyon effects on the mixing of air pollution was not considered on which we will make effort in the future.

The comparison between observations and predictions showed that the hybrid model significantly improved the underestimation of near-source concentrations due to grid dilution on emissions in CMAQ model. The implementation of the urban thermodynamic schemes in the hybrid model also relieved the overestimation in night-

time NO$_2$ concentrations from the CMAQ directly coupled with RLINE model. The predictions from CMAQ-RLINE_URBAN model could accurately reflect not only the impact of road local emissions, but also the pollution characteristics of non-vehicle sources at regional level. It revealed that in summer, the average contribution of vehicle emission to NO$_2$ concentrations in urban areas of Beijing was 11.8 μg/m^3, and the relative contribution accounted for approximately 39%. Moreover, the vehicle-induced NO$_2$ pollution increased significantly with the decreased distance to the road centerline, especially reaching 76 μg/m^3 (75%) on urban freeways.

On the basis of this study, the following perspectives are proposed for future research: (1) At present, considering the running cost, the grid resolution of area in Beijing 5th ring road and its surroundings can reach 50 m×50 m. We will make efforts to develop a parallel computing method to reduce the computing time, in order to improve the grid resolution of a relatively large-scale simulation. (2) In our study, a simplified two-reaction scheme was incorporated into the model to characterize the photochemical process of NO$_x$, since it performed similar predictions and less computational time compared with those of the complicated CB05 gas phase chemical mechanism (Kim et al., 2018). However, another study pointed that the impact of nonlinear O$_3$-NO$_x$-VOC chemistry on NO$_2$ concentrations in the deep canyon was nonnegligible (Zhong et al., 2017). The influence of different chemistry schemes on near-road simulation will be investigated in the future. (3) The long-term site-observation of wind environment and pollutant concentrations in various street canyons were suggested to be compared with modelling results, especially in deep street canyons with large aspect ratio. The navigation monitoring technology would be applied in the model verification, which can carry out large-scale observation of concentration along streets. (4) Here, we considered the dynamic impact of idealized building structure on wind environment in street canyons. However, there are many other influencing factors, such as building layout and arrangement, roof shape, green vegetation, and thermodynamic effect, which are suggested to be considered in future studies. (5) In this study, we mainly focused on the NO$_2$ concentrations. In fact, the concentration of particulate matter, especially UFP, will also have an obvious peak near the road centerline. In the future, the process of physical and chemical changes of particulate matter near the vehicle exhaust outlet should be further investigated.

Data availability

Data are available upon request from the corresponding author Huan Liu (liu_env@tsinghua.edu.cn).

Code availability

The RF and MARS model for MLSCF are both available on Github (https://github.com/claus0224/MLSCF-RF-MARS), and other codes are available from the corresponding author on reasonable request.

Acknowledgment

We would like to acknowledgment professor Jian Hang from Sun Yat-sen University for supports for CFD simulations and Dr. Jaime Benavides from Barcelona Supercomputing Center for the application of urban thermodynamic schemes. This work is supported by the National Natural Science Foundation of China (grant nos. 41822505 and 42061130213 to H.L.), the Tsinghua−Toyota General Research Center. H.L. is supported by the Royal Society of the United Kingdom through a Newton Advanced Fellowship (NAF\R1\201166).

Author contributions

Z. Lv and Z. Luo contributed equally. Z. Lv and Z. Luo designed the research and wrote the manuscript. H.L., Y.Z. and K.H. provided guidance on the research and revised the paper. Z. Lv, Z. Luo, and F.D. provided multiple analytical perspective on this research. X.W., J.Z., and L.X. helped collect and clean the data. T.H. helped on language modification.

Competing interests

The authors declare that they have no conflict of interest.

Additional information

The supplement is available for this paper at online resources.

Correspondence and requests for materials should be addressed to H.L.

References

Aleksankina, K., Reis, S., Vieno, M., and Heal, M. R.: Advanced methods for uncertainty assessment and global sensitivity analysis of an Eulerian atmospheric chemistry transport model, Atmospheric Chemistry and Physics, 19, 2881-2898, 2019.

An, Z., Huang, R.-J., Zhang, R., Tie, X., Li, G., Cao, J., Zhou, W., Shi, Z., Han, Y., Gu, Z., and Ji, Y.: Severe haze in northern China: A synergy of anthropogenic emissions and atmospheric processes, Proceedings of the National Academy of Sciences of the United States of America, 116, 8657-8666, 10.1073/pnas.1900125116, 2019.

Beddows, A. V., Kitwiroon, N., Williams, M. L., and Beevers, S. D.: Emulation and Sensitivity Analysis of the Community Multiscale Air Quality Model for a UK Ozone Pollution Episode, Environmental Science & Technology, 51, 6229-6236, 10.1021/acs.est.6b05873, 2017.

Benavides, J., Snyder, M., Guevara, M., Soret, A., Pérez García-Pando, C., Amato, F., Querol, X., and Jorba, O.: CALIOPE-Urban v1.0: coupling R-LINE with a mesoscale air quality modelling system for urban air quality forecasts over Barcelona city (Spain), Geosci. Model Dev., 12, 2811-2835, 10.5194/gmd-12-2811-2019, 2019.

Berchet, A., Zink, K., Muller, C., Oettl, D., Brunner, J., Emmenegger, L., and Brunner, D.: A cost-effective method for simulating city-wide air flow and pollutant dispersion at building resolving scale, Atmospheric Environment, 158, 181-196, https://doi.org/10.1016/j.atmosenv.2017.03.030, 2017.

Breiman, L.: Random Forests, Machine Learning, 45, 5-32, 10.1023/A:1010933404324, 2001.

Brown, M., Lawson, R., DeCroix, D., and Lee, R.: COMPARISON OF CENTERLINE VELOCITY MEASUREMENTS OBTAINED AROUND 2D AND 3D BUILDING ARRAYS IN A WIND TUNNEL, 2001.

Byun, D. and Schere, K. L.: Review of the Governing Equations, Computational Algorithms, and Other Components of the Models-3 Community Multiscale Air Quality (CMAQ) Modeling System, Applied Mechanics Reviews, 59, 51-77, 10.1115/1.2128636, 2006.

Chang, S. Y., Vizuete, W., Valencia, A., Naess, B., Isakov, V., Palma, T., Breen, M., and Arunachalam, S.: A modeling framework for characterizing near-road air pollutant concentration at community scales, Science of the Total Environment, 538, 905-921, 2015.

Chen, G., Li, S., Knibbs, L. D., Hamm, N. A., Cao, W., Li, T., Guo, J., Ren, H., Abramson, M. J., and Guo, Y.: A machine learning method to estimate PM2. 5 concentrations across China with remote sensing, meteorological and land use information, Science of the Total Environment, 636, 52-60, 2018.

Cheng, J., Su, J., Cui, T., Li, X., Dong, X., Sun, F., Yang, Y., Tong, D., Zheng, Y., Li, Y., Li, J., Zhang, Q., and He, K.: Dominant role of emission reduction in PM2.5 air quality improvement in Beijing during 2013–2017: a model-based decomposition analysis, Atmos. Chem. Phys., 19, 6125-6146, 10.5194/acp-19-6125-2019, 2019.

Cimorelli, A. J., Perry, S. G., Venkatram, A., Weil, J. C., Paine, R. J., Wilson, R. B., Lee, R. F., Peters, W. D., and Brode, R. W.: AERMOD: A Dispersion Model for Industrial Source Applications. Part I: General Model Formulation and Boundary Layer Characterization, Journal of Applied Meteorology, 44, 682-693, 10.1175/JAM2227.1, 2005.

Conibear, L., Reddington, C. L., Silver, B. J., Chen, Y., Knote, C., Arnold, S. R., and Spracklen, D. V.: Statistical Emulation of Winter Ambient Fine Particulate Matter Concentrations From Emission Changes in China, GeoHealth, 5, e2021GH000391, https://doi.org/10.1029/2021GH000391, 2021.

Cui, Y., Wang, L., Jiang, L., Liu, M., Wang, J., Shi, K., and Duan, X.: Dynamic spatial analysis of NO2 pollution over China: Satellite observations and spatial convergence models, Atmospheric Pollution Research, 12, 89-99, https://doi.org/10.1016/j.apr.2021.02.003, 2021.

Dejoan, A., Santiago, J., Martilli, A., Martin, F., and Pinelli, A.: Comparison between large-eddy simulation and Reynolds-averaged Navier–Stokes computations for the MUST field experiment. Part II: effects of incident wind angle deviation on the mean flow and plume dispersion, Boundary-layer meteorology, 135, 133-150, 2010.

Fang, K.-T., Li, R., and Sudjianto, A.: Design and modeling for computer experiments, Chapman and Hall/CRC2005.

Filigrana, P., Milando, C., Batterman, S., Levy, J. I., Mukherjee, B., and Adar, S. D.: Spatiotemporal variations in traffic activity and their influence on air pollution levels in communities near highways, Atmospheric Environment, 242, 117758, https://doi.org/10.1016/j.atmosenv.2020.117758, 2020.

FLUENT: FLUENT V6.3. User's Manual. Available online: http://www.fluent.com (accessed on 20 August 2017). 2006.

Foken, T.: 50 Years of the Monin–Obukhov Similarity Theory, Boundary-Layer Meteorology, 119, 431-447, 10.1007/s10546-006-9048-6, 2006.

Franke, J., Hellsten, A., Schlunzen, K. H., and Carissimo, B.: The COST 732 Best Practice Guideline for CFD simulation of flows in the urban environment: a summary, International Journal of Environment and Pollution, 44, 419-427,

616 10.1504/IJEP.2011.038443, 2011.

617 Friedman, J. H.: Multivariate adaptive regression splines, The annals of statistics, 19, 1-67, 1991.

618 Fu, X., Liu, J., Ban-Weiss, G. A., Zhang, J., Huang, X., Ouyang, B., Popoola, O., and Tao, S.: Effects of canyon geometry on
619 the distribution of traffic-related air pollution in a large urban area: Implications of a multi-canyon air pollution dispersion
620 model, Atmospheric Environment, 165, 111-121, https://doi.org/10.1016/j.atmosenv.2017.06.031, 2017.

621 Geng, G., Meng, X., He, K., and Liu, Y.: Random forest models for PM2. 5 speciation concentrations using MISR fractional
622 AODs, Environmental Research Letters, 15, 034056, 2020.

623 Grell, G. A., Peckham, S. E., Schmitz, R., McKeen, S. A., Frost, G., Skamarock, W. C., and Eder, B.: Fully coupled "online"
624 chemistry within the WRF model, Atmospheric Environment, 39, 6957-6975, https://doi.org/10.1016/j.atmosenv.2005.04.027,
625 2005.

626 Hagler, G. S. W., Thoma, E. D., and Baldauf, R. W.: High-Resolution Mobile Monitoring of Carbon Monoxide and Ultrafine
627 Particle Concentrations in a Near-Road Environment, Journal of the Air & Waste Management Association, 60, 328-336,
628 10.3155/1047-3289.60.3.328, 2012.

629 Hang, J., Sandberg, M., Li, Y., and Claesson, L.: Flow mechanisms and flow capacity in idealized long-street city models,
630 Building and Environment, 45, 1042-1053, https://doi.org/10.1016/j.buildenv.2009.10.014, 2010.

631 He, J., Wu, L., Mao, H., Liu, H., Jing, B., Yu, Y., Ren, P., Feng, C., and Liu, X.: Development of a vehicle emission inventory
632 with high temporal–spatial resolution based on NRT traffic data and its impact on air pollution in Beijing – Part 2: Impact of
633 vehicle emission on urban air quality, Atmos. Chem. Phys., 16, 3171-3184, 10.5194/acp-16-3171-2016, 2016.

634 Heist, D., Isakov, V., Perry, S., Snyder, M., Venkatram, A., Hood, C., Stocker, J., Carruthers, D., Arunachalam, S., and Owen,
635 R. C.: Estimating near-road pollutant dispersion: A model inter-comparison, Transportation Research Part D: Transport and
636 Environment, 25, 93-105, 2013.

637 Hood, C., MacKenzie, I., Stocker, J., Johnson, K., Carruthers, D., Vieno, M., and Doherty, R.: Air quality simulations for
638 London using a coupled regional-to-local modelling system, Atmos. Chem. Phys., 18, 11221-11245, 10.5194/acp-18-11221-
639 2018, 2018.

640 Hu, X., Belle, J. H., Meng, X., Wildani, A., Waller, L. A., Strickland, M. J., and Liu, Y.: Estimating PM2. 5 concentrations in
641 the conterminous United States using the random forest approach, Environmental science & technology, 51, 6936-6944, 2017.

642 Jensen, S. S., Ketzel, M., Becker, T., Christensen, J., Brandt, J., Plejdrup, M., Winther, M., Nielsen, O.-K., Hertel, O., and
643 Ellermann, T.: High resolution multi-scale air quality modelling for all streets in Denmark, Transportation Research Part D:
644 Transport and Environment, 52, 322-339, https://doi.org/10.1016/j.trd.2017.02.019, 2017.

645 Jin, Y., Andersson, H., and Zhang, S.: Air Pollution Control Policies in China: A Retrospective and Prospects, International
646 Journal of Environmental Research and Public Health, 13, 1219, 2016.

647 Kakosimos, K. E., Hertel, O., Ketzel, M., and Berkowicz, R.: Operational Street Pollution Model (OSPM) – a review of
648 performed application and validation studies, and future prospects, Environmental Chemistry, 7, 485-503,
649 https://doi.org/10.1071/EN10070, 2010.

650 Kamińska, J. A.: A random forest partition model for predicting NO2 concentrations from traffic flow and meteorological
651 conditions, Science of the Total Environment, 651, 475-483, 2019.

652 Ke, W., Zhang, S., Wu, Y., Zhao, B., Wang, S., and Hao, J.: Assessing the Future Vehicle Fleet Electrification: The Impacts on
653 Regional and Urban Air Quality, Environmental Science & Technology, 51, 1007-1016, 10.1021/acs.est.6b04253, 2017.

654 Keller, C. A. and Evans, M. J.: Application of random forest regression to the calculation of gas-phase chemistry within the
655 GEOS-Chem chemistry model v10, Geoscientific Model Development, 12, 1209-1225, 2019.

656 Ketzel, M., Jensen, S., Brandt, J., Ellermann, T., Berkowicz, R., and Hertel, O.: Evaluation of the street pollution model OSPM
657 for measurement at 12 street stations using using newly developed and freely available evaluation tool, J. Civil. Environ. Eng.,

658 2012.

659 Khaniabadi, Y. O., Goudarzi, G., Daryanoosh, S. M., Borgini, A., Tittarelli, A., and De Marco, A.: Exposure to PM10, NO2,
660 and O3 and impacts on human health, Environmental Science and Pollution Research, 24, 2781-2789, 10.1007/s11356-016-
661 8038-6, 2017.

662 Kheirbek, I., Haney, J., Douglas, S., Ito, K., and Matte, T.: The contribution of motor vehicle emissions to ambient fine
663 particulate matter public health impacts in New York City: a health burden assessment, Environmental Health, 15, 89,
664 10.1186/s12940-016-0172-6, 2016.

665 Kikumoto, H., Ooka, R., Sugawara, H., and Lim, J.: Observational study of power-law approximation of wind profiles within
666 an urban boundary layer for various wind conditions, Journal of Wind Engineering and Industrial Aerodynamics, 164, 13-21,
667 https://doi.org/10.1016/j.jweia.2017.02.003, 2017.

668 Kim, Y., Wu, Y., Seigneur, C., and Roustan, Y.: Multi-scale modeling of urban air pollution: development and application of a
669 Street-in-Grid model (v1.0) by coupling MUNICH (v1.0) and Polair3D (v1.8.1), Geosci. Model Dev., 11, 611-629,
670 10.5194/gmd-11-611-2018, 2018.

671 Lefebvre, W., Van Poppel, M., Maiheu, B., Janssen, S., and Dons, E.: Evaluation of the RIO-IFDM-street canyon model chain,
672 Atmospheric Environment, 77, 325-337, https://doi.org/10.1016/j.atmosenv.2013.05.026, 2013.

673 Liaw, A., Wiener, M. : Classification and regression by randomForest, R News, 2, 18–22, 2002.

674 Lien, F.-S. and Yee, E.: Numerical Modelling of the Turbulent Flow Developing Within and Over a 3-D Building Array, Part
675 I: A High-Resolution Reynolds-Averaged Navier—Stokes Approach, Boundary-Layer Meteorology, 112, 427-466,
676 10.1023/B:BOUN.0000030654.15263.35, 2004.

677 Luo, Z., Xu, H., Zhang, Z., Zheng, S., and Liu, H.: Year-round changes in tropospheric nitrogen dioxide caused by COVID-
678 19 in China using satellite observation, Journal of Environmental Sciences, https://doi.org/10.1016/j.jes.2022.01.013, 2022a.

679 Luo, Z., Wang, Y., Lv, Z., He, T., Zhao, J., Wang, Y., Gao, F., Zhang, Z., and Liu, H.: Impacts of vehicle emission on air quality
680 and human health in China, Science of The Total Environment, 813, 152655, https://doi.org/10.1016/j.scitotenv.2021.152655,
681 2022b.

682 Lv, Z., Wang, X., Deng, F., Ying, Q., Archibald, A. T., Jones, R. L., Ding, Y., Cheng, Y., Fu, M., Liu, Y., Man, H., Xue, Z., He,
683 K., Hao, J., and Liu, H.: Source–Receptor Relationship Revealed by the Halted Traffic and Aggravated Haze in Beijing during
684 the COVID-19 Lockdown, Environmental Science & Technology, 54, 15660-15670, 10.1021/acs.est.0c04941, 2020.

685 Greenwell B M.: pdp: An R Package for Constructing Partial Dependence Plots, R Journal, 9(1): 421., 2017.

686 Mallet, V., Tilloy, A., Poulet, D., Girard, S., and Brocheton, F.: Meta-modeling of ADMS-Urban by dimension reduction and
687 emulation, Atmospheric Environment, 184, 37-46, https://doi.org/10.1016/j.atmosenv.2018.04.009, 2018.

688 Manning, A. J., Nicholson, K. J., Middleton, D. R., and Rafferty, S. C.: Field Study of Wind and Traffic to Test a Street Canyon
689 Pollution Model, Environmental Monitoring and Assessment, 60, 283-313, 10.1023/A:1006187301966, 2000.

690 Masey, N., Hamilton, S., and Beverland, I. J.: Development and evaluation of the RapidAir® dispersion model, including the
691 use of geospatial surrogates to represent street canyon effects, Environmental Modelling & Software, 108, 253-263,
692 https://doi.org/10.1016/j.envsoft.2018.05.014, 2018.

693 Mu, Q., Denby, B. R., Wærsted, E. G., and Fagerli, H.: Downscaling of air pollutants in Europe using uEMEP_v6, Geosci.
694 Model Dev., 15, 449-465, 10.5194/gmd-15-449-2022, 2022.

695 Murena, F., Favale, G., Vardoulakis, S., and Solazzo, E.: Modelling dispersion of traffic pollution in a deep street canyon:
696 Application of CFD and operational models, Atmospheric Environment, 43, 2303-2311,
697 https://doi.org/10.1016/j.atmosenv.2009.01.038, 2009.

698 Nayeb Yazdi, M., Delavarrafiee, M., and Arhami, M.: Evaluating near highway air pollutant levels and estimating emission
699 factors: Case study of Tehran, Iran, Science of The Total Environment, 538, 375-384,

https://doi.org/10.1016/j.scitotenv.2015.07.141, 2015.

Nguyen, C., Soulhac, L., and Salizzoni, P.: Source Apportionment and Data Assimilation in Urban Air Quality Modelling for NO2: The Lyon Case Study, Atmosphere, 9, 10.3390/atmos9010008, 2018.

Oke, T. R.: Street design and urban canopy layer climate, Energy and Buildings, 11, 103-113, https://doi.org/10.1016/0378-7788(88)90026-6, 1988.

Pandey, J. S., Kumar, R., and Devotta, S.: Health risks of NO2, SPM and SO2 in Delhi (India), Atmospheric Environment, 39, 6868-6874, https://doi.org/10.1016/j.atmosenv.2005.08.004, 2005.

Patterson, R. F. and Harley, R. A.: Evaluating near-roadway concentrations of diesel-related air pollution using RLINE, Atmospheric Environment, 199, 244-251, https://doi.org/10.1016/j.atmosenv.2018.11.016, 2019.

Reichstein, M., Camps-Valls, G., Stevens, B., Jung, M., Denzler, J., Carvalhais, N., and Prabhat: Deep learning and process understanding for data-driven Earth system science, Nature, 566, 195-204, 10.1038/s41586-019-0912-1, 2019.

Santiago, J., Dejoan, A., Martilli, A., Martin, F., and Pinelli, A.: Comparison between large-eddy simulation and Reynolds-averaged Navier–Stokes computations for the MUST field experiment. Part I: study of the flow for an incident wind directed perpendicularly to the front array of containers, Boundary-Layer Meteorology, 135, 109-132, 2010.

Shah, V., Jacob, D. J., Li, K., Silvern, R. F., Zhai, S., Liu, M., Lin, J., and Zhang, Q.: Effect of changing NOx lifetime on the seasonality and long-term trends of satellite-observed tropospheric NO2 columns over China, Atmos. Chem. Phys., 20, 1483-1495, 10.5194/acp-20-1483-2020, 2020.

Snyder, M. G., Venkatram, A., Heist, D. K., Perry, S. G., Petersen, W. B., and Isakov, V.: RLINE: A line source dispersion model for near-surface releases, Atmospheric Environment, 77, 748-756, https://doi.org/10.1016/j.atmosenv.2013.05.074, 2013.

Soulhac, L., Perkins, R. J., and Salizzoni, P.: Flow in a Street Canyon for any External Wind Direction, Boundary-Layer Meteorology, 126, 365-388, 10.1007/s10546-007-9238-x, 2008.

Soulhac, L., Nguyen, C., Volta, P., and Salizzoni, P.: The model SIRANE for atmospheric urban pollutant dispersion. PART III: Validation against NO 2 yearly concentration measurements in a large urban agglomeration, Atmospheric Environment, 167, 10.1016/j.atmosenv.2017.08.034, 2017.

Soulhac, L., Salizzoni, P., Mejean, P., Didier, D., and Rios, I.: The model SIRANE for atmospheric urban pollutant dispersion; PART II, validation of the model on a real case study, Atmospheric Environment, 49, 320-337, https://doi.org/10.1016/j.atmosenv.2011.11.031, 2012.

Stocker, J., Hood, C., Carruthers, D., and McHugh, C.: ADMS-Urban: developments in modelling dispersion from the city scale to the local scale, International Journal of Environment and Pollution, 50, 308-316, 10.1504/IJEP.2012.051202, 2012.

Tominaga, Y., Mochida, A., Yoshie, R., Kataoka, H., Nozu, T., Yoshikawa, M., and Shirasawa, T.: AIJ guidelines for practical applications of CFD to pedestrian wind environment around buildings, Journal of Wind Engineering and Industrial Aerodynamics, 96, 1749-1761, https://doi.org/10.1016/j.jweia.2008.02.058, 2008.

Valencia, A., Venkatram, A., Heist, D., Carruthers, D., and Arunachalam, S.: Development and evaluation of the R-LINE model algorithms to account for chemical transformation in the near-road environment, Transportation Research Part D: Transport and Environment, 59, 464-477, 2018.

Vara-Vela, A., Andrade, M. F., Kumar, P., Ynoue, R. Y., and Muñoz, A. G.: Impact of vehicular emissions on the formation of fine particles in the Sao Paulo Metropolitan Area: a numerical study with the WRF-Chem model, Atmos. Chem. Phys., 16, 777-797, 10.5194/acp-16-777-2016, 2016.

Xie, Z. and Castro, I. P.: LES and RANS for turbulent flow over arrays of wall-mounted obstacles, Flow, Turbulence and Combustion, 76, 291-312, 2006.

Yu, M., Zhu, Y., Lin, C.-J., Wang, S., Xing, J., Jang, C., Huang, J., Huang, J., Jin, J., and Yu, L.: Effects of air pollution control

measures on air quality improvement in Guangzhou, China, Journal of Environmental Management, 244, 127-137, https://doi.org/10.1016/j.jenvman.2019.05.046, 2019.

Zhai, X., Russell, A. G., Sampath, P., Mulholland, J. A., Kim, B.-U., Kim, Y., and D'Onofrio, D.: Calibrating R-LINE model results with observational data to develop annual mobile source air pollutant fields at fine spatial resolution: Application in Atlanta, Atmospheric Environment, 147, 446-457, 2016.

Zhang, K., Chen, G., Wang, X., Liu, S., Mak, C. M., Fan, Y., and Hang, J.: Numerical evaluations of urban design technique to reduce vehicular personal intake fraction in deep street canyons, Science of The Total Environment, 653, 968-994, https://doi.org/10.1016/j.scitotenv.2018.10.333, 2019a.

Zhang, Q., Tong, P., Liu, M., Lin, H., Yun, X., Zhang, H., Tao, W., Liu, J., Wang, S., Tao, S., and Wang, X.: A WRF-Chem model-based future vehicle emission control policy simulation and assessment for the Beijing-Tianjin-Hebei region, China, Journal of Environmental Management, 253, 109751, https://doi.org/10.1016/j.jenvman.2019.109751, 2020.

Zhang, Q., Zheng, Y., Tong, D., Shao, M., Wang, S., Zhang, Y., Xu, X., Wang, J., He, H., Liu, W., Ding, Y., Lei, Y., Li, J., Wang, Z., Zhang, X., Wang, Y., Cheng, J., Liu, Y., Shi, Q., Yan, L., Geng, G., Hong, C., Li, M., Liu, F., Zheng, B., Cao, J., Ding, A., Gao, J., Fu, Q., Huo, J., Liu, B., Liu, Z., Yang, F., He, K., and Hao, J.: Drivers of improved PM$_{2.5}$ air quality in China from 2013 to 2017, Proceedings of the National Academy of Sciences, 116, 24463-24469, 10.1073/pnas.1907956116, 2019b.

Zhang, X., Just, A. C., Hsu, H.-H. L., Kloog, I., Woody, M., Mi, Z., Rush, J., Georgopoulos, P., Wright, R. O., and Stroustrup, A.: A hybrid approach to predict daily NO2 concentrations at city block scale, Science of The Total Environment, 761, 143279, https://doi.org/10.1016/j.scitotenv.2020.143279, 2021a.

Zhang, Y., Ye, X., Wang, S., He, X., Dong, L., Zhang, N., Wang, H., Wang, Z., Ma, Y., Wang, L., Chi, X., Ding, A., Yao, M., Li, Y., Li, Q., Zhang, L., and Xiao, Y.: Large-eddy simulation of traffic-related air pollution at a very high resolution in a mega-city: evaluation against mobile sensors and insights for influencing factors, Atmos. Chem. Phys., 21, 2917-2929, 10.5194/acp-21-2917-2021, 2021b.

Zheng, B., Tong, D., Li, M., Liu, F., Hong, C., Geng, G., Li, H., Li, X., Peng, L., Qi, J., Yan, L., Zhang, Y., Zhao, H., Zheng, Y., He, K., and Zhang, Q.: Trends in China's anthropogenic emissions since 2010 as the consequence of clean air actions, Atmos. Chem. Phys., 18, 14095-14111, 10.5194/acp-18-14095-2018, 2018.

Zhong, J., Cai, X.-M., and Bloss, W. J.: Coupling dynamics and chemistry in the air pollution modelling of street canyons: A review, Environmental Pollution, 214, 690-704, https://doi.org/10.1016/j.envpol.2016.04.052, 2016.

Zhong, J., Cai, X.-M., and Bloss, W. J.: Large eddy simulation of reactive pollutants in a deep urban street canyon: Coupling dynamics with O3-NOx-VOC chemistry, Environmental Pollution, 224, 171-184, https://doi.org/10.1016/j.envpol.2017.01.076, 2017.

Zhu, Y., Zhan, Y., Wang, B., Li, Z., Qin, Y., and Zhang, K.: Spatiotemporally mapping of the relationship between NO2 pollution and urbanization for a megacity in Southwest China during 2005–2016, Chemosphere, 220, 155-162, https://doi.org/10.1016/j.chemosphere.2018.12.095, 2019.

778

779
780 **Figure 1: The framework of multiscale hybrid model CMAQ-RLINE_URBAN.**

781
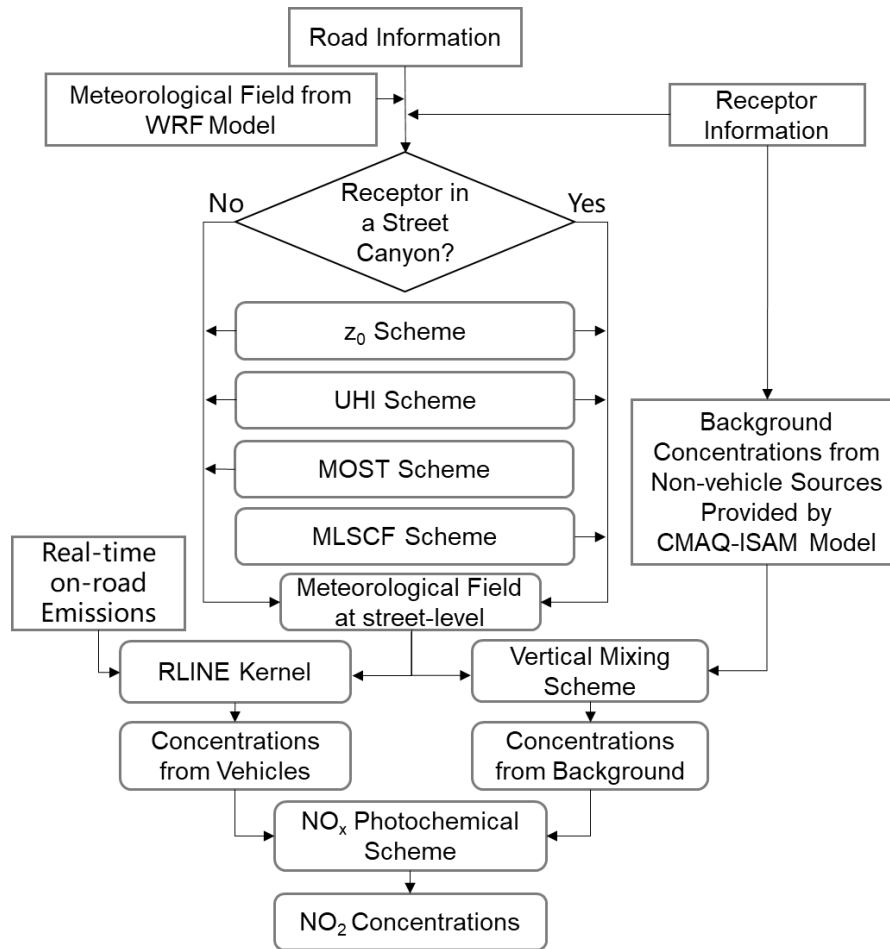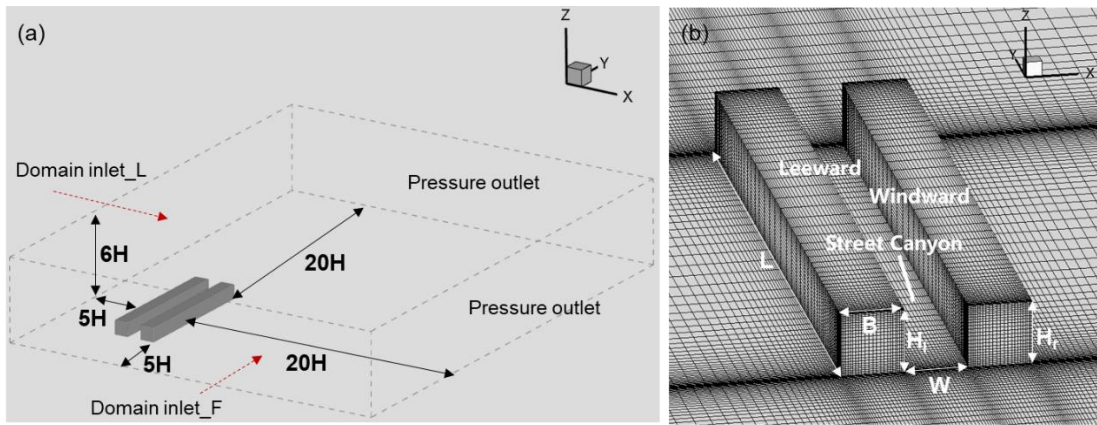
782
783 **Figure 2: Computational domain (a) and grid arrangement (b) in all CFD test case.**

784
785
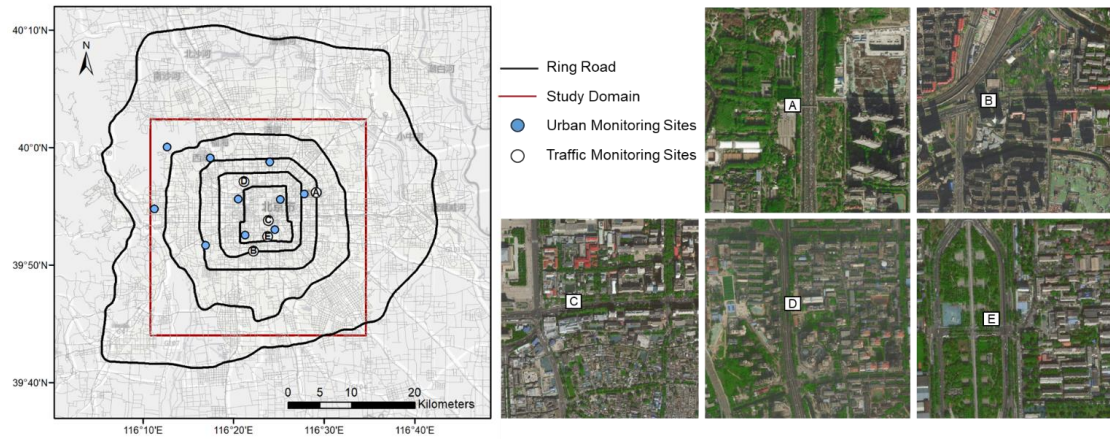
Figure 3: Study domain (© OpenStreetMap contributors 2020. Distributed under the Open Data Commons Open Database License (ODbL) v1.0) and location of monitoring sites (© Microsoft). A. DSH; B. NSH; C. QM; D. XZM; E. YDM.
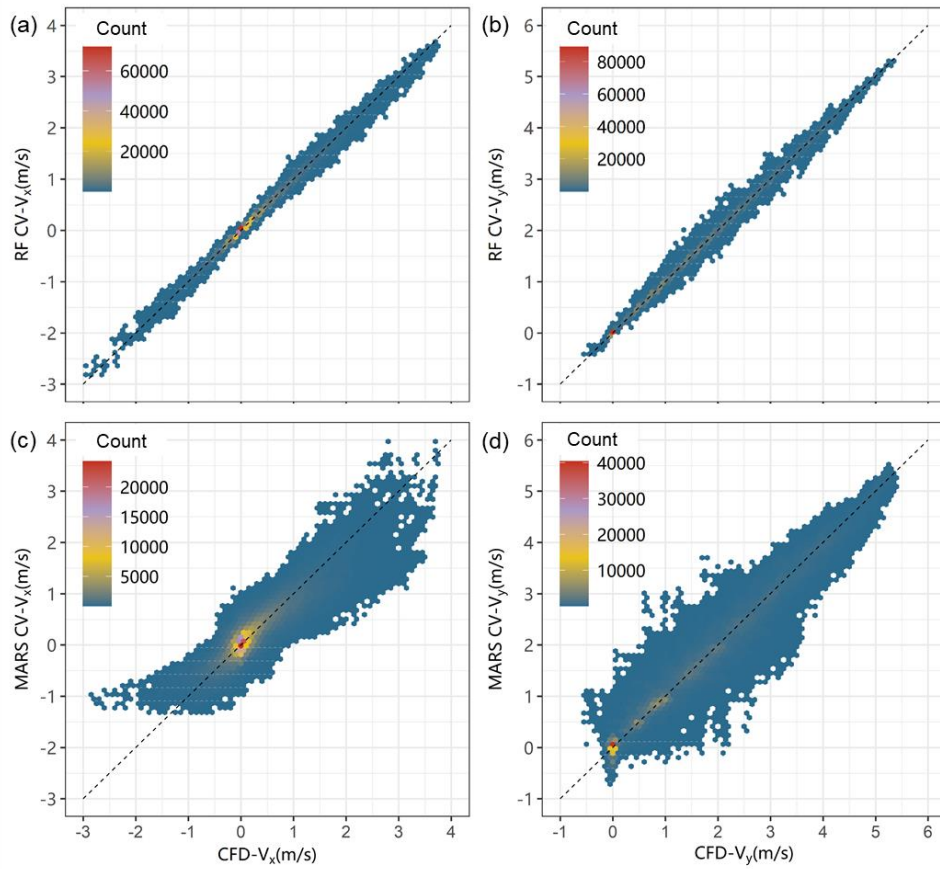
791
792 **Figure 4: Cross validations of machine learning models for Vx (a, c) and Vy (b, d): (a)-(b) RF model; (c)-(d)**

793 **MARS model.**

794
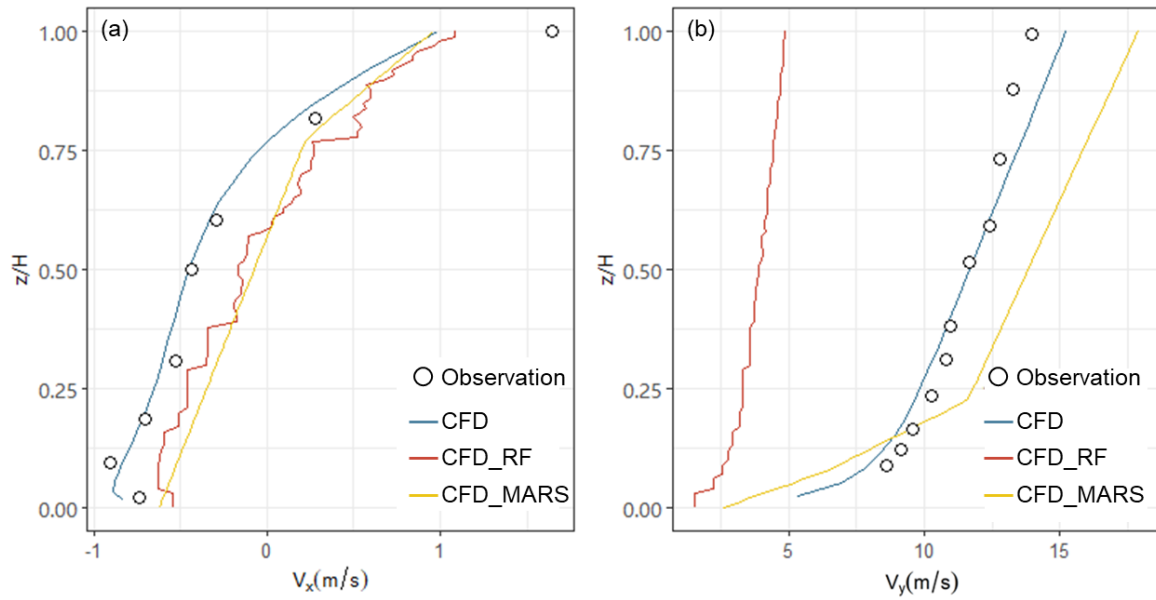
795
796 **Figure 5: Performances of machine learning on velocity profile in wind tunnel experiments. The street**
797 **canyon was perpendicular (a) or parallel (b) to the wind direction at the roof level in different experiments.**
798 **The detailed description of each experiment was introduced in Section 2.2.3.**
799
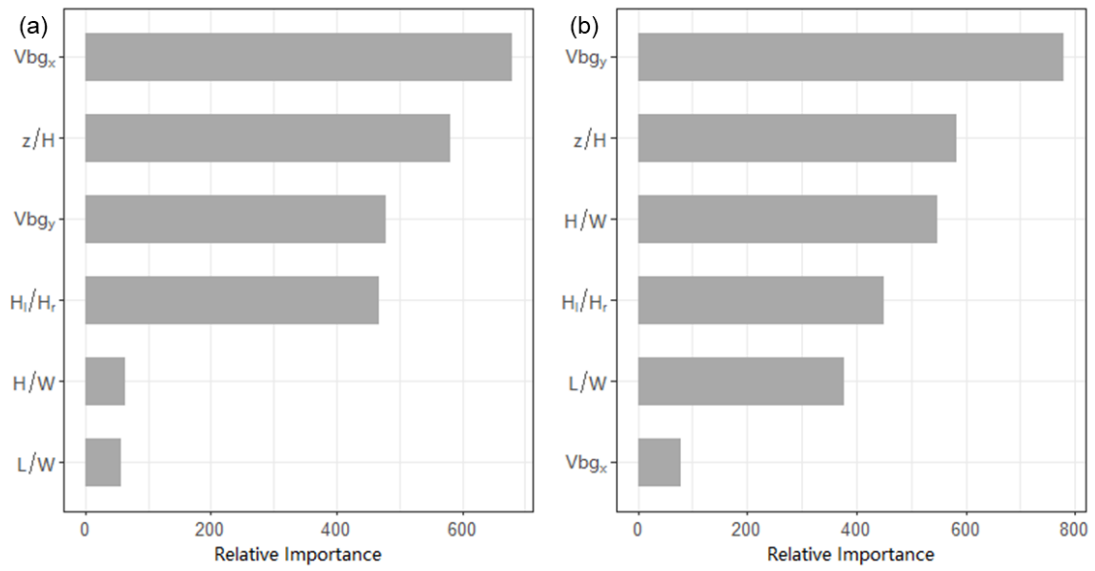
800

801 **Figure 6: Variable importance ranking in the RF model for (a) V_x and (b) V_y.**

802
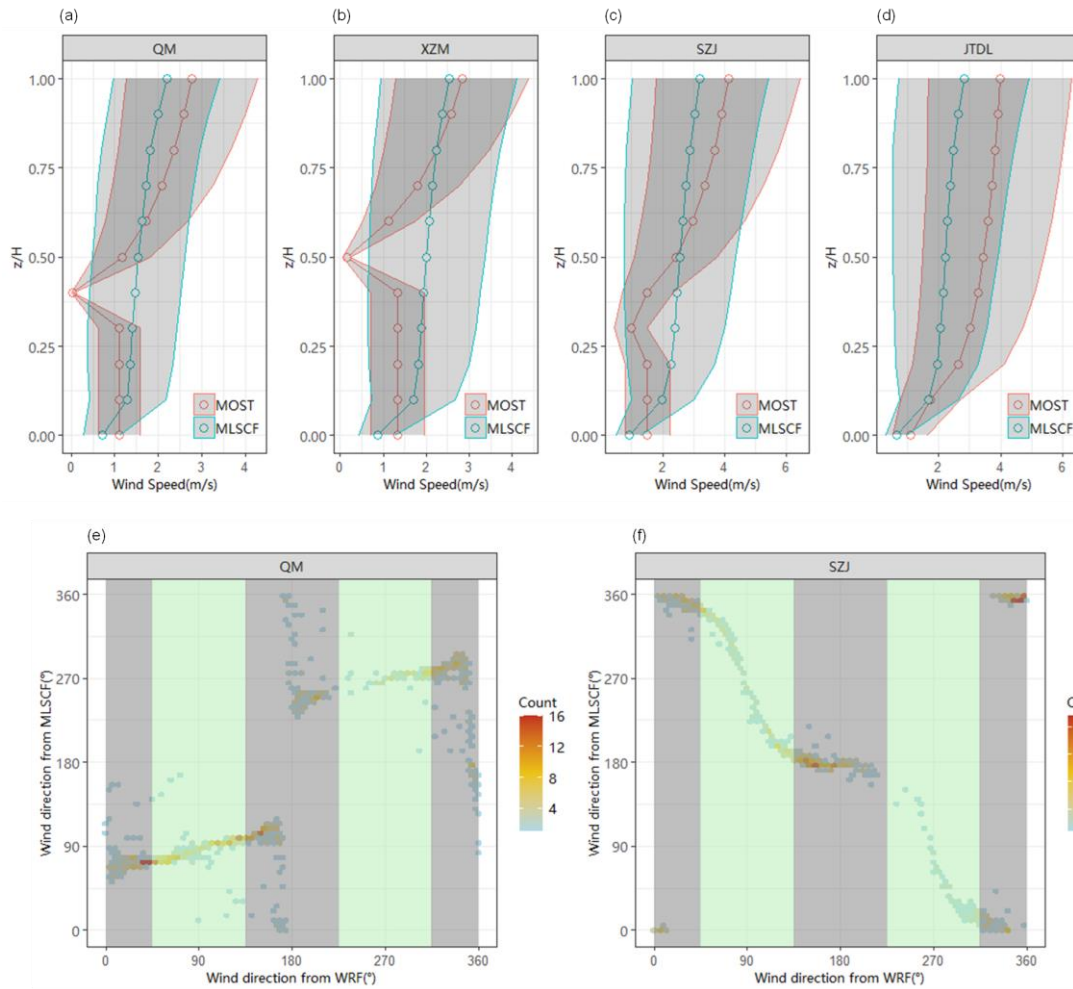
803
804 **Figure 7: Influence of MLSCF on wind filed in the street canyon. Monthly averaged vertical profile of wind**
805 **speed from MOST and MLSCF method in different street canyons: (a) QM (H/W=0.22); (b) XZM**
806 **(H/W=0.35); (c) SZJ (H/W=1); (b) JTDL (H/W=1.93). The gray shade represents the standard deviation in**
807 **results of all hours. Hourly wind direction from WRF model (at roof level) and MLSCF method (at ground**
808 **level) in different street canyons: (e) QM (H/W=0.22); (f) SZJ (H/W=1). As the gray and green shade shown,**
809 **the background wind over the street canyon provided by WRF model was divided into four main directions:**
810 **east, west, south and north.**
811

812
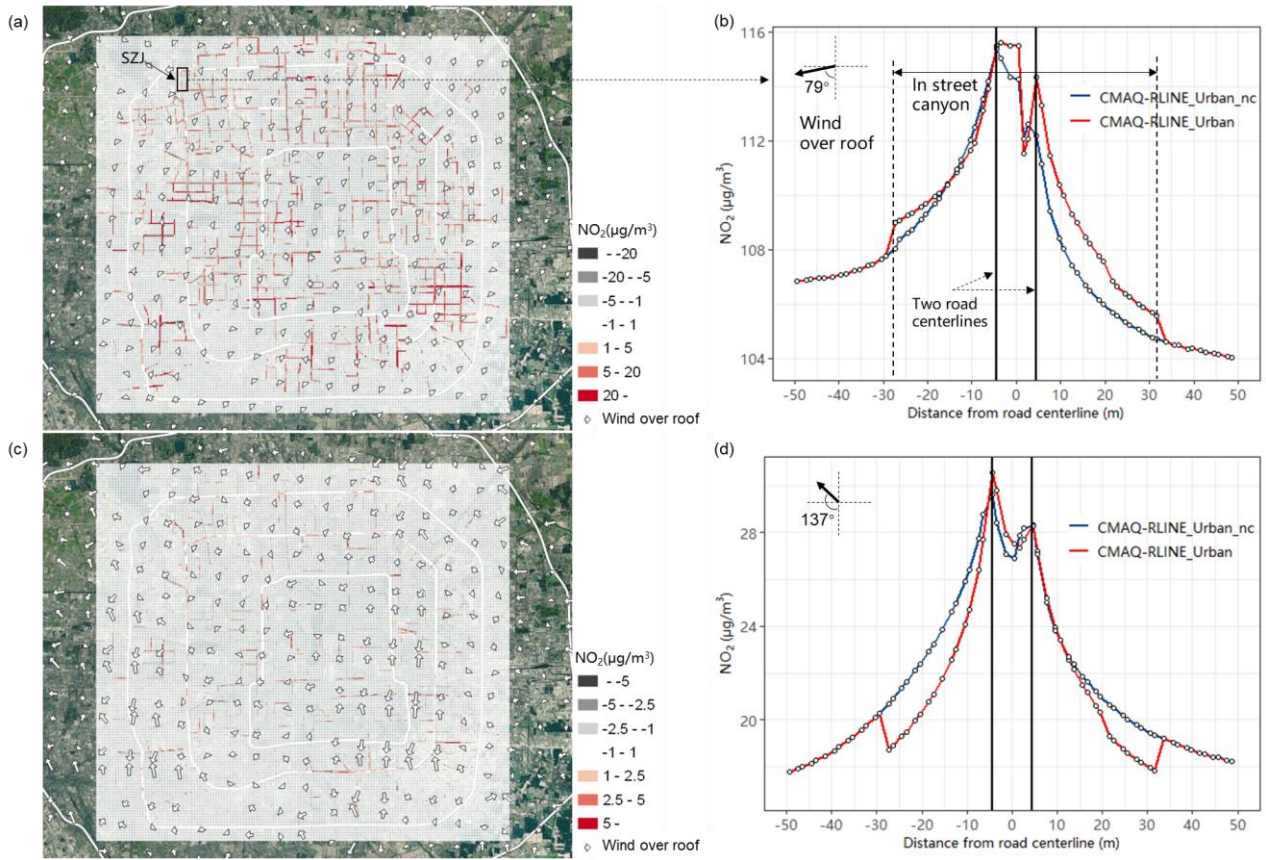
Figure 8: Differences in NO₂ concentrations at the height of 1.5 m impacted by MLSCF scheme (a, c) over

the study domain (CMAQ-RLINE_URBAN - CMAQ-RLINE_URBAN_nc) (© Microsoft) and (b, d) near

SZJ in 2019-08-24 at 0:00-1:00 (a, b) and 10:00-11:00 (c, d).

816

817
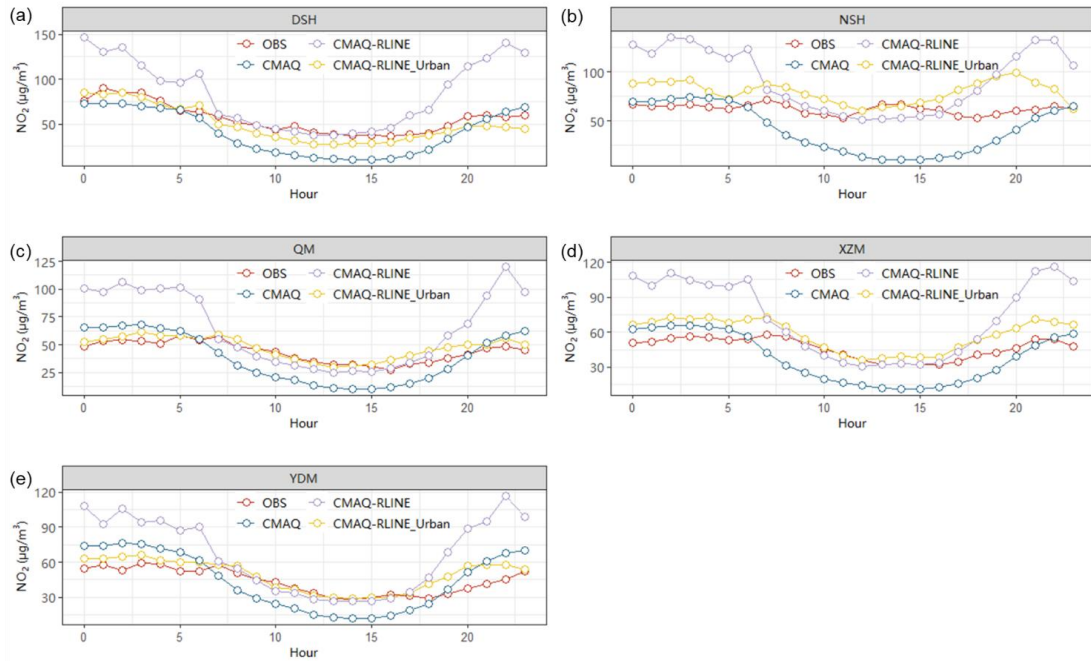
Figure 9: Diurnal variations of observed and predicted hourly averaged NO₂ concentrations from different

models at near-road monitoring sites: (a) DSH; (b) NSH; (c) QM; (d) XZM; (e) YDM.

820

821
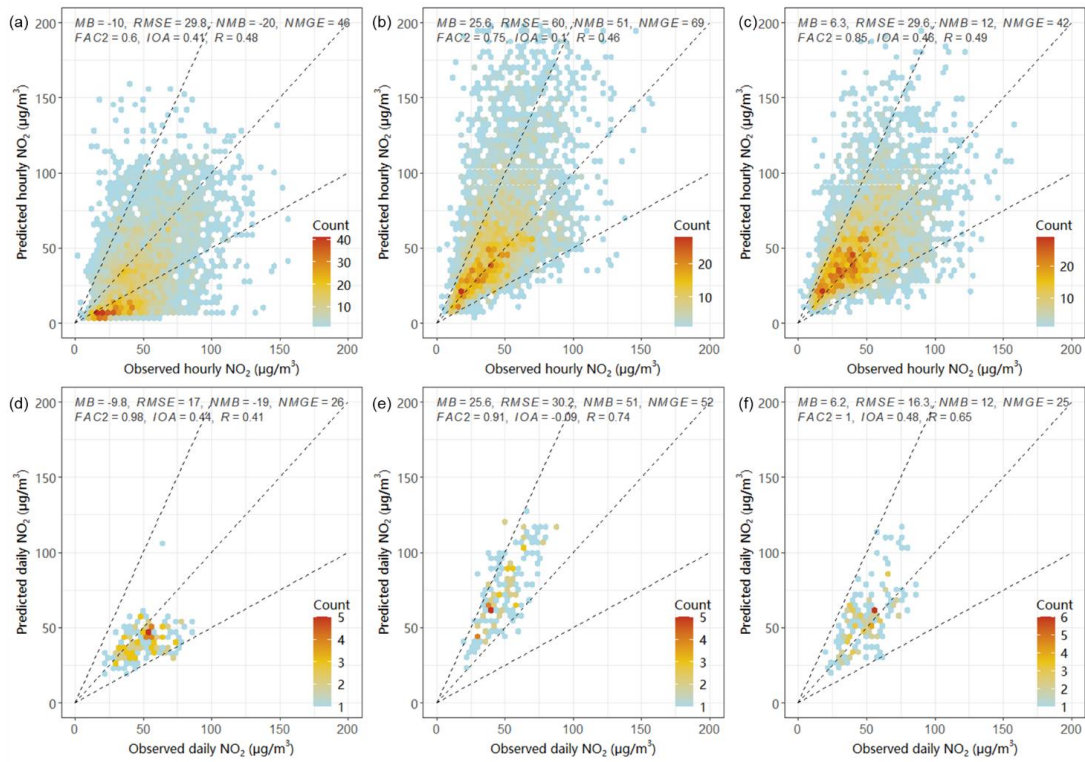
Figure 10: Observed and predicted hourly (a-c) or daily averaged (d-f) NO2 concentrations from different models at near-road sites: (a, d) CMAQ model; (b, e) CMAQ-RLINE model; (c, f) CMAQ-RLINE_URBAN model.

825

826
827
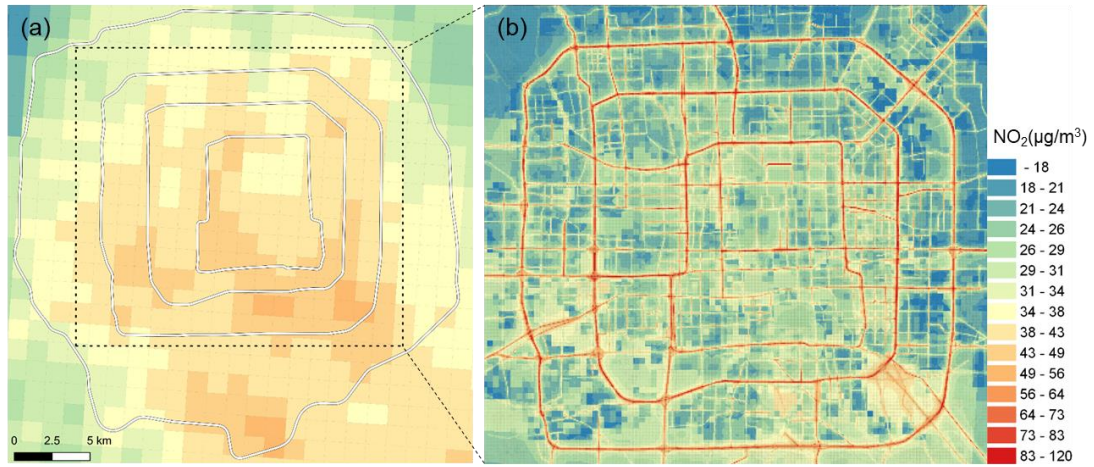
828
829 **Figure 11: Spatial distribution of monthly averaged NO₂ concentrations from (a) CMAQ model and (b)**

830 **CMAQ-RLINE_URBAN model.**

831
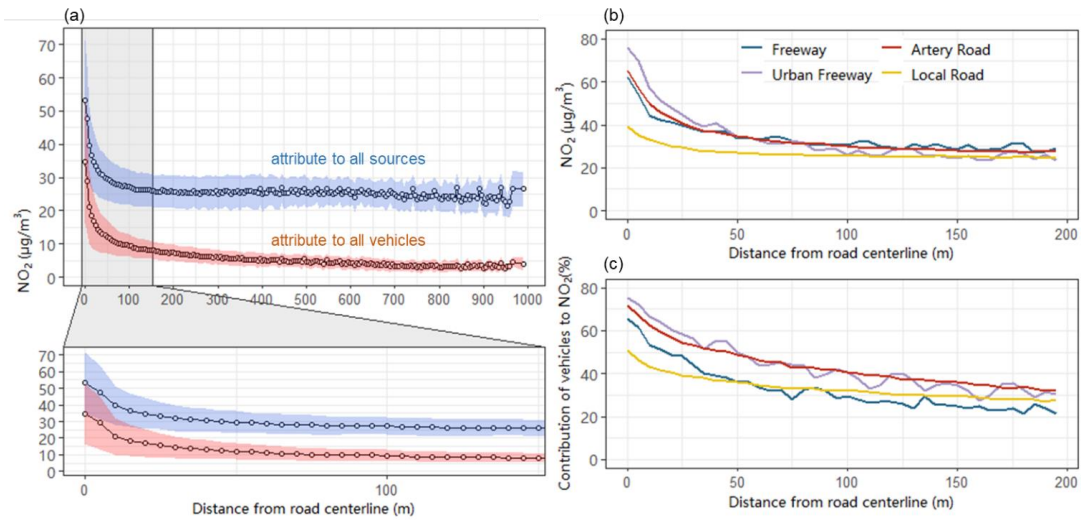
832
833 **Figure 12: Monthly averaged NO$_2$ concentrations attributed to all emission sources or vehicles with distance**

834 **from the receptor to its nearest road centerline. (a) NO$_2$ attributed to all emission sources near all roads; (b)**

835 **NO$_2$ attributed to all emission sources near different road types; (c) Relative contribution of vehicles to NO$_2$**

836 **near different road types. The shade area in (a) represents the standard deviation in results of all receptors.**

837

Table 1: Values of controlling factors used in the simulations.

Controlling factor	Value				
H_l/H_r (unitless)	0.50	0.75	1.00	1.33	2.00
H/W (unitless)	0.25	0.50	1.00	2.00	-
L/H (unitless)	3	5	10	20	-
$V(H)$ (m/s)	1	2	3	4	5
α (°)	0	30	60	90	-

Table 2: Model performances under different scenarios

Sites	Scenario	MB	RMSE	NMB	NMGE	FAC2	IOA	*R*
	CMAQ	3.1	25.6	9	53	0.65	0.45	0.52
All	CMAQ-RLINE	18.5	46.6	53	77	0.67	0.19	0.55
	CMAQ-RLINE_URBAN	4.6	25.8	13	49	0.75	0.49	0.57
	CMAQ	8.0	24.3	27	58	0.68	0.40	0.59
Urban	CMAQ-RLINE	12.3	35.8	43	76	0.64	0.20	0.50
	CMAQ-RLINE_URBAN	1.3	23.1	4	51	0.71	0.47	0.49

*MB: Mean bias; RSME: Root mean squared error; NMB: Normalized mean bias; NMGE: Normalized mean gross error; FAC2: Fraction of predictions within a factor of two; IOA: Index of agreement; R: correlation coefficient.